EUMETSAT Satellite Application Facility on Climate Monitoring

The EUMETSAT Network of Satellite Application Facilities

CM SAF
Climate Monitoring

CM SAF Cloud, Albedo, Radiation dataset, AVHRR-based, Edition 1 (CLARA-A1)

Cloud Physical Products

Algorithm Theoretical Basis Document

Cloud optical thickness	**CM-34**
Cloud Phase	**CM-38**
Liquid water path	**CM-43**
Ice water path	**CM-47**

Reference Number:	SAF/CM/KNMI/ATBD/GAC/CPP
Issue/Revision Index:	1.1
Date:	23.04.2012

Document Signature Table

	Name	Function	Signature	Date
Author	Jan Fokke Meirink Rob Roebeling Erwin Wolters	CM-SAF scientists		23/04/2012
Editor	Rainer Hollmann	Science Coordinator		05/05/2012
Approval	Steering Group			26/09/2012
Release	Martin Werscheck	SAF Manager		30/11/2012

Distribution List

Internal Distribution		
Name		**No. Copies**
DWD Archive Team	CM-SAF	1 1

External Distribution		
Company	**Name**	**No. Copies**
PUBLIC		

Document Change Record

Issue/ Revision	Date	DCN No.	Changed Pages/Paragraphs
1.0	21/11/2011	SAF/CM/KNMI/ATBD/GAC/CPP	Initial release prepared for DRI5
1.1	23/04/2012	SAF/CM/KNMI/ATBD/GAC/CPP	Updated version in response to DRI5 review comments - editorial update of cover page to account for DOI number and edition name - editorial update of the introduction section of CM SAF

Applicable documents

Reference	Title	Code
AD-1	CDOP Product Requirements Document	SAF/CM/DWD/PRD/1.7

Reference documents

Reference	Title	Code
RD-1	ATBD for SAFNWC/PPS "Cloud Mask" (CM-PGE01 v3.1)	SAF/NWC/CDOP/SMHI-PPS/SCI/ATBD/1
RD-2	ATBD for SAFNWC/PPS "Cloud Top Temperature and Height" (CTTH-PGE03 v3.1)	SAF/NWC/CDOP/SMHI-PPS/SCI/ATBD/3

Table of Contents

1. The EUMETSAT SAF on Climate Monitoring

The importance of climate monitoring with satellites was recognized in 2000 by EUMETSAT Member States when they amended the EUMETSAT Convention to affirm that the EUMETSAT mandate is also to "contribute to the operational monitoring of the climate and the detection of global climatic changes". Following this, EUMETSAT established within its Satellite Application Facility (SAF) network a dedicated centre, the SAF on Climate Monitoring (CM SAF, http://www.cmsaf.eu).

The consortium of CM SAF currently comprises the Deutscher Wetterdienst (DWD) as host institute, and the partners from the Royal Meteorological Institute of Belgium (RMIB), the Finnish Meteorological Institute (FMI), the Royal Meteorological Institute of the Netherlands (KNMI), the Swedish Meteorological and Hydrological Institute (SMHI), the Meteorological Service of Switzerland (MeteoSwiss), and the Meteorological Service of the United Kingdom (UK MetOffice). Since the beginning in 1999, the EUMETSAT Satellite Application Facility on Climate Monitoring (CM SAF) has developed and will continue to develop capabilities for a sustained generation and provision of Climate Data Records (CDR's) derived from operational meteorological satellites.

In particular the generation of long-term data sets is pursued. The ultimate aim is to make the resulting data sets suitable for the analysis of climate variability and potentially the detection of climate trends. CM SAF works in close collaboration with the EUMETSAT Central Facility and liaises with other satellite operators to advance the availability, quality and usability of Fundamental Climate Data Records (FCDRs) as defined by the Global Climate Observing System (GCOS). As a major task the CM-SAF utilizes FCDRs to produce records of Essential Climate Variables (ECVs) as defined by GCOS. Thematically, the focus of CM SAF is on ECVs associated with the global energy and water cycle.

Another essential task of CM SAF is to produce data sets that can serve applications related to the new Global Framework of Climate Services initiated by the WMO World Climate Conference-3 in 2009. CM SAF is supporting climate services at national meteorological and hydrological services (NMHSs) with long-term data records but also with data sets produced close to real time that can be used to prepare monthly/annual updates of the state of the climate. Both types of products together allow for a consistent description of mean values, anomalies, variability and potential trends for the chosen ECVs. CM SAF ECV data sets also serve the improvement of climate models both at global and regional scale.

As an essential partner in the related international frameworks, in particular WMO SCOPE-CM (Sustained COordinated Processing of Environmental satellite data for Climate Monitoring), the CM SAF - together with the EUMETSAT Central Facility, assumes the role as main implementer of EUMETSAT's commitments in support to global climate monitoring. This is achieved through:

- Application of highest standards and guidelines as lined out by GCOS for the satellite data processing,
- Processing of satellite data within a true international collaboration benefiting from developments at international level and pollinating the partnership with own ideas and standards,

- Intensive validation and improvement of the CM SAF climate data records,
- Taking a major role in data set assessments performed by research organisations such as WCRP. This role provides the CM SAF with deep contacts to research organizations that form a substantial user group for the CM SAF CDRs,
- Maintaining and providing an operational and sustained infrastructure that can serve the community within the transition of mature CDR products from the research community into operational environments.

A catalogue of all available CM SAF products is accessible via the CM SAF webpage, www.cmsaf.eu/. Here, detailed information about product ordering, add-on tools, sample programs and documentation is provided.

2. Introduction

This CM-SAF Algorithm Theoretical Basis Document (ATBD) provides detailed information on the retrieval algorithm that has been used to derive a thematic climate data record (TCDR) of cloud physical products (CPP) from GAC-AVHRR measurements. Disseminated products are daily and monthly cloud optical thickness (COT), cloud thermodynamic phase (CPH), cloud liquid water path (LWP) and ice water path (IWP). Table 1 shows the corresponding product numbers.

Table 1: Overview of CM-SAF products covered in this ATBD.

Product	Product number
COT	CM-34
CPH	CM-38
LWP	CM-43
IWP	CM-47

The algorithm description in this document is largely based on Roebeling (2008). The CPP algorithm and products have been used for many studies (e.g., Roebeling et al. 2006, 2008; Wolters et al. 2008; Roebeling and Van Meijgaard 2009; Greuell and Roebeling 2009; Wolters et al. 2010; Greuell et al. 2011).

The cloud physical properties retrieval algorithms are run for cloudy pixels only. The selection of cloudy pixels is done on the basis of the NWC-SAF cloud mask, also used in the CM-SAF for the determination of cloud fraction (RD-1).

In Section 3 an overview of the retrieval algorithms is presented. Section 4 gives a detailed description of the retrieval algorithms, consisting of the relevant underlying physics (Section 4.1), the radiative transfer modelling (Section 4.2), the implementation of the retrieval scheme (Section 4.3), the error budget of the retrieved products (Section 4.4), and the practical application of the algorithms (Section 4.5). Finally, assumptions and limitations are discussed in Section 5.

3. Algorithm Overview

The CPP (cloud physical properties) algorithm, developed at KNMI, retrieves cloud optical thickness at visible wavelengths (COT or τ), cloud particle effective radius (r_e), cloud thermodynamic phase (CPH), and liquid/ice/total cloud water path (LWP/IWP/CWP). COT, CPH, and CWP are produced both for geostationary (MSG-SEVIRI) and polar-orbiting (NOAA/METOP-AVHRR and similar) imagers. The retrieval scheme was first described in Roebeling et al. (2006), and is based on earlier methods that retrieve cloud optical thickness and cloud particle effective radius from satellite radiances at wavelengths in the non-absorbing visible and the moderately absorbing solar infrared part of the spectrum (Nakajima and King 1990; Han et al. 1994; Nakajima and Nakajima 1995; Watts et al. 1998).

4. Algorithm description

4.1. Theoretical description

The principle of the CPP retrieval algorithm is that the reflectance of clouds at a non-absorbing wavelength in the visible region (VIS: 0.6 or 0.8 μm) is strongly related to the optical thickness and has little dependence on particle size, whereas the reflectance of clouds at an absorbing wavelength in the near-infrared region (NIR: 1.6 or 3.7 μm) is primarily related to particle effective radius. Moreover, Figure 1 shows that the imaginary parts of the refractive indices of water and ice, which are a measure for absorption, differ. For example, around 1.6 and 3.7 μm ice particles are more absorbing than water droplets. This feature, together with the use of a thermal infrared (IR) window channel to inform on cloud-top temperature, allows to retrieve cloud thermodynamic phase.

The cloud optical thickness is defined at 0.6 μm under the assumption of a plane parallel atmosphere with reference to a vertical transect. The particle effective radius is given by the ratio of the volume to the projected area, and is the relevant quantity for radiative scattering. In case of a collection of spherical water droplets, the effective radius is defined as:

$$ r_e = \frac{\int_0^\infty r \pi r^2 n(r) dr}{\int_0^\infty \pi r^2 n(r) dr}, \qquad (1) $$

where r is the radius of the particle, and $n(r)$ dr is the number of particles per unit volume with radius between r and $r+dr$. For ice clouds, a multitude of definitions exist (e.g., McFarquhar and Heymsfield 1998); our approach to ice crystals is outlined in Section 4.2.

Liquid Water Path (LWP) is computed from the retrieved τ and r_e by (Stephens 1978):

$$ LWP = \frac{2}{3} \tau r_e \rho_l, \qquad (2) $$

where ρ_l = 1 g cm^{-3} is the density of water. Ice Water Path (IWP) is computed analogously, but using the density of ice, ρ_i = 0.93 g cm^{-3}.
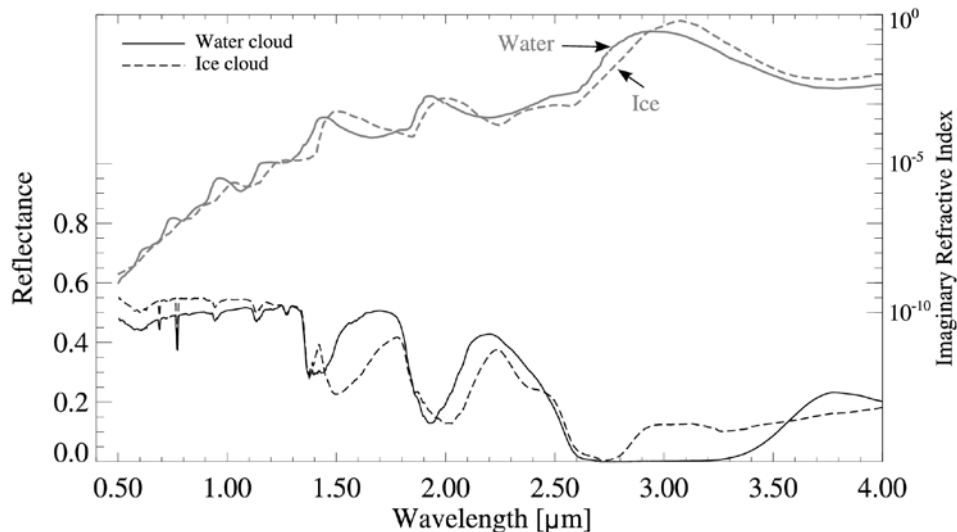
Figure 1: Simulated top-of-atmosphere (TOA) reflectance spectra for a stratocumulus (water) cloud and a cirrus (ice) cloud, and the imaginary part of the index of refraction of water and ice. The simulations were made with MODTRAN at $\theta_0 = 45°$, $\theta = 0°$ and $\varphi = 0°$. The reflectances are plotted as black lines, while the refractive indices are plotted as gray lines.

4.2. Radiative transfer

The CPP algorithm compares satellite observed reflectances at visible and near-infrared wavelengths to look-up tables (LUTs) of simulated reflectances for given cloud optical thicknesses, particle sizes and surface albedos for water and ice clouds (Watts et al. 1998; Jolivet and Feijt 2003). The Doubling Adding KNMI (DAK) radiative transfer model has been used to generate the LUTs of simulated cloud reflectances. DAK has been developed for line-by-line or monochromatic multiple scattering calculations at UV, visible and near infrared wavelengths in a horizontally homogeneous cloudy atmosphere using the doubling-adding method (De Haan et al. 1987; Stammes 2001). The clouds are assumed to be plane-parallel and embedded in a multi-layered Rayleigh scattering atmosphere. The particles of water clouds are assumed to be spherical droplets with effective radii between 1 and 24 μm and an effective variance of 0.15. For ice clouds, homogeneous distributions of imperfect hexagonal ice crystals (Hess et al. 1998) are assumed with volume equivalent effective radii between 6 and 51 μm. The volume equivalent effective radius is defined as the effective radius the hexagonal columns would have if their columnar volume were converted into a perfect sphere. Knap et al. (2005) demonstrated that these crystals give adequate simulations of total and polarized reflectances of ice clouds.

Figure 2 shows an example of DAK calculations of 0.6 and 1.6 μm reflectances as function of τ and r_e for water droplets and ice crystals. The figure illustrates that for optically thick clouds ($\tau > 16$) lines of equal τ and particle size are nearly orthogonal, meaning that the 0.6 and 1.6 μm reflectances contain independent information on τ and r_e, respectively. This is not the case for optically thin clouds. Moreover, for these clouds, the lines of different r_e are very close together, implying that the retrieval of particle size is inherently uncertain. Finally, comparing the two panels in Figure 2, it is evident that ice clouds have a lower 1.6-μm reflectance than water clouds, which is a consequence of the stronger absorption of ice

particles compared to water droplets at the 1.6 µm wavelength (Knap et al. 1999; Jolivet and Feijt 2003).

Plots as in Figure 2 look similar for other channel combinations, e.g. with 0.8 µm as non-absorbing wavelength or 3.7 µm as absorbing wavelength. There are, however, significant differences. At 3.7 µm the absorption by water and especially ice is much stronger than at 1.6 µm. As a result, the dynamical range of reflectance is lower, but lines of equal τ and r_e are more orthogonal.
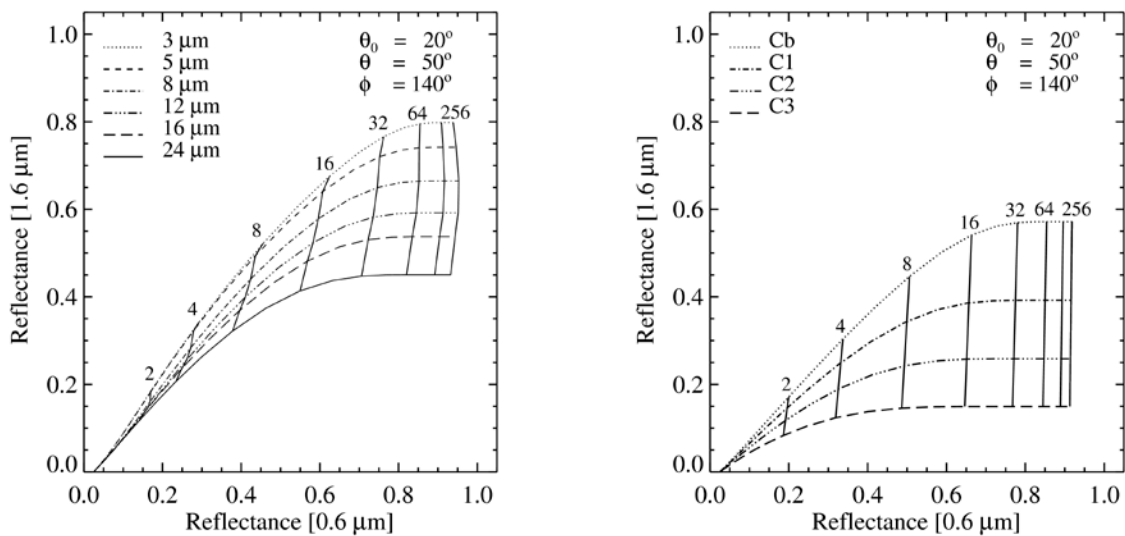
Figure 2: DAK calculations of TOA reflectance at 0.6 µm versus 1.6 µm for clouds consisting of spherical water droplets with effective radii between 3 and 24 µm (left panel) and imperfect hexagonal ice columns Cb, C1, C2 and C3 (right panel). The reflectances have been calculated over a black surface (albedo = 0). Solar and satellite angles are indicated in the plots. The vertically oriented lines represent lines of equal cloud optical thicknesses between 0 and 256, while the horizontally oriented lines represent lines of equal particle size.

Table 2: Properties of the cloudy atmosphere that are used for the radiative transfer calculations to generate the LUTs.

Parameter	*Settings*	
Vertical profiles of pressure, temperature, and ozone	Midlatitude summer [a]	
Aerosol model	None	
Cloud height	1000 - 2000 m	
Solar zenith angle (θ_0) [b]	0 - 78.7° ($\approx$equidistant in $\mu_0 = \cos(\theta_0)$, 65 points)	
Viewing zenith angle (θ) [b]	Same as θ_0	
Relative azimuth angle (ϕ) [b]	0 - 180° (equidistant, 91 points)	
Cloud optical thickness	0 – 256 (equidistant in $\log(\tau)$, 22 points)	
	water clouds	**ice clouds**
Cloud particle type	Spherical water droplet	Imperfect hexagonal ice crystal [c]

			Type	D (μm)	L (μm)	r_e (μm)
Cloud particle size	1 –24 μm (1, 3, 5, 8, 12, 16, 24 μm)					
			Cb	4.0	10.0	6.0
			C1	10.0	30.0	12.0
			C2	22.0	60.0	26.0
			C3	41.0	130.0	51.0
Liquid / Ice water path	0 – 4,096 g m^{-2}		0 – 8,704 g m^{-2}			
Size distribution	Two-parameter gamma		-			
Effective variance (v_e)	0.15		-			

[a] The midlatitude summer atmosphere model was taken from Anderson et al. (1986).

[b] The chosen distributions of angles are motivated in Wolters et al. (2006).

[c] The imperfect hexagonal crystals are obtained from Hess et al. (1998) and have a distortion angle of 30°. The crystals are characterized by their length (L), diameter (D) and volume equivalent effective radius (r_e).

[d] This value is within the range found from in situ measurements. Different choices are possible, but the impact on the retrieved cloud properties is modest

Table 2 summarizes the governing characteristics of the cloudy atmosphere, together with information about intervals of cloud properties and viewing geometries used in the DAK simulations to generate the LUT. The DAK simulations were done for a black surface. The TOA reflectance $R(\alpha_s)$ over a surface with reflectance α_s is computed using (Chandrasekhar, 1960):

$$R(\alpha_S) = R(\alpha_S = 0) + \frac{\alpha_s t_c(\theta_0) t_c(\theta)}{1 - \alpha_s \alpha_a} \qquad (3)$$

Here, $t_c(\theta_0)$ and $t_c(\theta)$ are the cloud transmissivity at the solar and viewing zenith angles, respectively, and α_a is the hemispherical sky albedo for upwelling, isotropic radiation. The required parameters are determined from two additional DAK calculations with surface reflectance values of 0.5 and 1.0.

The DAK calculations concern monochromatic radiative transfer at a wavelength close to the center of the respective satellite imager narrowbands. These calculations neglect scattering and absorption by atmospheric gases, except for Rayleigh scattering by air molecules and absorption by ozone. Before the reflectance simulated by DAK can be compared to an observed reflectance, the absorption by atmospheric gases in the band has to be taken into account. This so-called atmospheric correction has been implemented based on MODTRAN4.2 (Berk et al. 2000) radiative transfer simulations. The atmosphere-corrected TOA reflectance ($R_{atm.corr.}$) is calculated as:

$$R_{atm.corr.} = R\, t_{a,ac}(\theta_0, H_c, WVP)\, t_{a,ac}(\theta, H_c, WVP), \qquad (4)$$

where $t_{a,ac}$ is the above-cloud atmospheric transmissivity simulated by MODTRAN using a Lambertian surface placed at the cloud top height $\backslash H_c$) and for a given water vapor path (WVP). The two-way transmissivity, i.e. the product of the two transmissivities in Eq. (4), is a function of the geometrical air mass factor (AMF = $1/\mu_0 + 1/\mu$). This two-way transmissivity is stored in a LUT with dimensions AMF, H_c, and WVP. Absorption by trace gases within and below the cloud is neglected. An indication of the magnitude of the atmospheric correction is given in Table 3.

Table 3: Typical magnitude of atmospheric correction, expressed as 1 minus the two-way transmissivity, in %. The numbers have been calculated for a reference atmosphere (H_c = 2 km, AMF = 2, and WVP = 30 kg m^{-2}), based on the NOAA-15 AVHRR spectral response, and for individual absorbing gases as well as for all gases together.

Gas	Channel 1	Channel 3a	Channel 3b
H_2O	0.6 %	0.2 %	11.9 %
O_3	0.7 %	-	-
O_2	0.1 %	-	-
CO_2		3.1 %	0.2 %
CH_4		0.1 %	3.7 %
N_2O			1.6 %
N_2-continuum			0.7 %
All gases	1.5 %	3.4 %	17.6 %

More details on the implementation of atmospheric correction and the effect on retrieved cloud properties can be found in Meirink et al. (2009).

Whereas at 1.6 μm reflected sunlight is the only significant component of the measured TOA radiance, at 3.7 μm thermal emission by the surface, atmosphere and clouds provides a non-negligible contribution. Thermal emission is expressed as a reflectance (R_e), and calculated as the sum of contributions from surface ($R_{e,s}$) and cloud ($R_{e,c}$) following Nakajima and Nakajima (1995):

$$R_e = R_{e,s} + R_{e,c} = \left(\varepsilon_s B_\lambda(T_s) t_a(\theta) t_c(\theta) + \varepsilon_c B_\lambda(T_c) t_{a,ac}(\theta) \right) \frac{\pi}{\mu_0 F_{0,\lambda}}., \qquad (5)$$

where ε_s is the surface emissivity, T_s and T_c are the surface and cloud-top temperatures, respectively, $B_\lambda(T)$ is the Planck function at temperature T and wavelength λ (= 3.7 μm), $F_{0,\lambda}$ is the extraterrestrial solar flux at wavelength λ, and ε_c is the cloud emissivity approximated as:

$$\varepsilon_c = 1 - t_c(\theta_0) - R(\theta_0, \theta, \phi). \qquad (6)$$

ε_c is a function of τ and r_e through the cloud transmissivity t_c and reflectivity R. The retrieval procedure is the same as for the 1.6-μm channel with the observed 3.7-μm radiance converted to a reflectance which is compared with the sum of simulated reflected sunlight and thermal emission.

4.3. Retrieval scheme

The cloud optical thickness and particle size are retrieved for cloudy pixels in an iterative manner as illustrated in Figure 3. During the iteration the retrieval of τ at the 0.6-μm channel

is used to update the retrieval of r_e at the 1.6/3.7-μm channel. This iteration process continues until the retrieved cloud physical properties converge to stable values. The interpolation between cloud physical properties in the LUTs is done with polynomial interpolation for τ and linear interpolation for r_e. As stated above, the retrieved particle size values are unreliable for optically thin clouds. Therefore for thin clouds the retrieved effective radius is adjusted towards an assumed climatologically averaged effective radius of 8 μm and 26 μm for water and ice clouds, respectively, values that are close to the ones used by Rossow and Schiffer (1999). The adjustment is performed for clouds with $\tau < 8$ using a smooth weighting function that gives an increasing weight to the climatologically averaged effective radius with decreasing cloud optical thickness. At 3.7 μm the adjustment of r_e is applied for $\tau < 5$ because there is more information on r_e for thin clouds in this channel due to the stronger absorption.
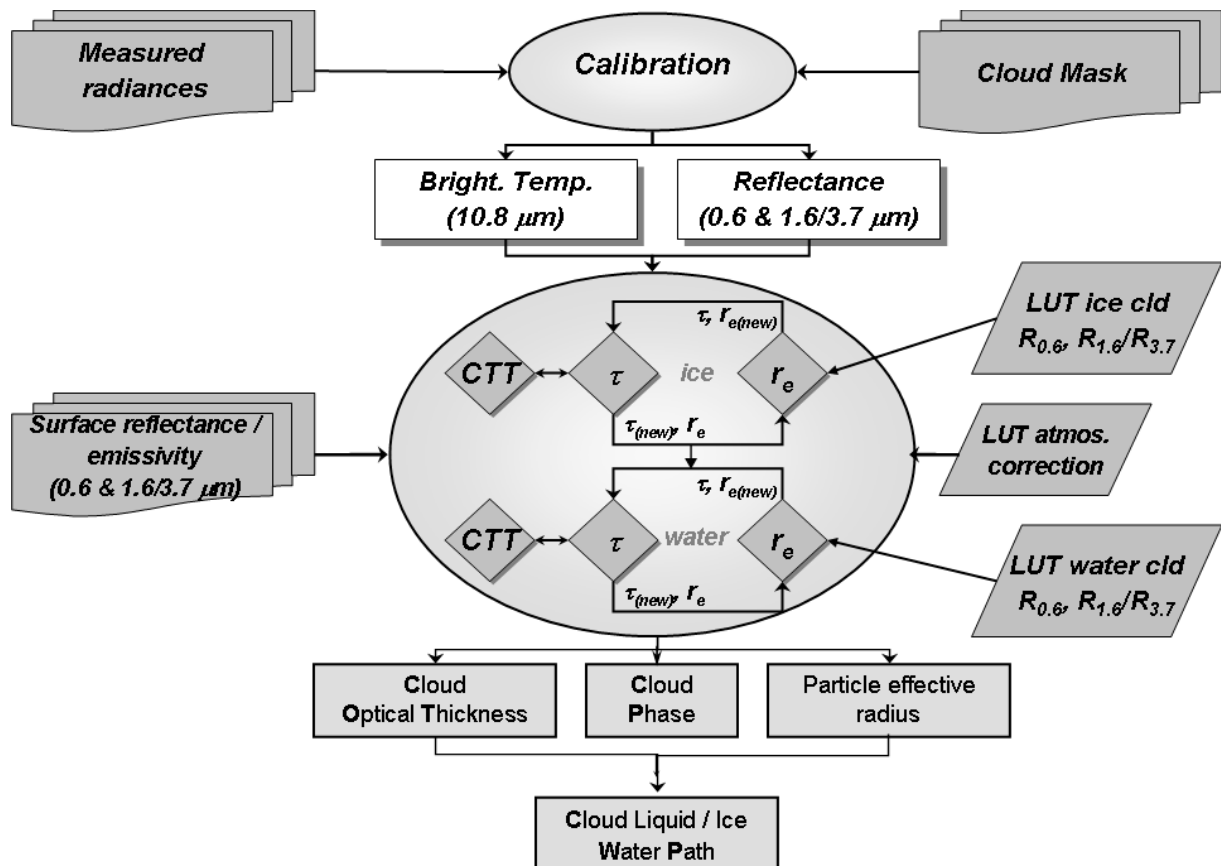

Figure 3: Flowchart of CPP algorithm for determining cloud phase, τ, r_e, LWP and IWP using lookup tables of DAK-simulated 0.6- and 1.6/3.7-μm reflectances, cloud-top temperatures derived from 10.8-μm brightness temperatures and τ, an atmospheric correction LUT created with MODTRAN, and ancillary data including surface reflectivity and emissivity.

The cloud thermodynamic phase (CPH) is determined as follows. The iterative process described above is first applied using the ice cloud LUT. If convergence is achieved and the cloud-top temperature (T_c) is lower than 265 K, the phase 'ice' is assigned. If not, the phase 'water' is assigned, and the iterative process to find τ and r_e is applied using the water cloud LUT.

The cloud-top temperature is calculated from the 11-μm brightness temperature and the cloud emissivity. Similar to Eq. (5) the upwelling TOA radiance I_λ, has contributions from both the cloud and the surface below and can be approximated by:

$$I_\lambda = \varepsilon_{c,\lambda}\, B_\lambda(T_c) + (1 - \varepsilon_{c,\lambda})\, B_\lambda(T_s)\,, \qquad (7)$$

in which a surface emissivity of unity is assumed at 11 μm. In the absence of scattering, the cloud emissivity can be approximated as a function of the absorption optical thickness at wavelength λ (τ_λ) and the cosine of the satellite zenith angle (θ) as follows (Minnis et al. 1993):

$$\varepsilon_\lambda = 1 - \exp\left(\frac{-\tau_\lambda}{\cos\theta}\right). \qquad (8)$$

The (absorption) cloud optical thickness in the infrared (τ_{tir}) is related to the (scattering) cloud optical thickness in the visible (τ_{vis}). This relationship depends on particle size and thermodynamic phase. For large water and ice particles $\tau_{tir} \approx 0.5\,\tau_{vis}$ (Minnis et al. 1993). With ε_λ known, T_c is calculated from Equation (7).

4.4. Error budget estimates

The retrieval of cloud optical thickness and effective radius from 2-channel backscattered solar radiation is a simple but heavily underconstrained problem. As a result, many uncertainties are associated to this retrieval problem (see Stephens and Kummerow (2007) for a review). Here we attempt to describe some of the most important error sources. In Section 5, further sources of uncertainty related to violation of basic retrieval assumptions are discussed.

Errors in radiative transfer

To assess the potential error caused by uncertainties in radiative transfer modeling, Roebeling et al. (2005) compared four well-known RTMs that use different methods to solve the equation of radiative transfer. All these models are suited for simulating short-wave and narrow-band radiances in a cloudy atmosphere. However, the codes have originally been developed and optimized for different applications. The following methods for solving radiative transfer were compared:

- Monte Carlo method

The Monte Carlo model (Macke et al. 1999) is a forward scheme with a local estimate procedure for radiance calculations. It is a straightforward model that can be extended from one-dimensional to two- or three-dimensional calculations (Davis et al. 1985). Monte Carlo treats multiple scattering as a stochastic process. The phase function governs the probability of scattering in a specific direction. Photons are emitted by a source (e.g. the sun or a lidar device) and undergo scattering and absorption events inside a predefined three-dimensional cloudy atmosphere until: (i) the intensity of the photons falls below a certain threshold, (ii) the photons escape from the system, (iii) or the photons are absorbed by the atmosphere or the surface (forward scheme). After each scattering event, the intensity of the photons that contribute to predefined sensor viewing angles is calculated (local estimate procedure).

- Doubling Adding method

This is the method used in the DAK model introduced in Section 4.2. DAK first calculates the reflection and transmission of an optically thin layer, in which no more than two scattering events may occur. Thanks to this restriction the radiative transfer equation can be solved analytically. Next, the reflection and transmission of two identical layers on top of each other can be obtained by computing successive reflections back and forth between the layers. This doubling procedure is continued until the actual optical thickness of the cloud is reached. The cloud is embedded in a multilayer Rayleigh scattering atmosphere. The DAK model includes polarization.

- Discrete Ordinates method

In the MODerate spectral resolution atmospheric TRANsmittance and radiance code (MODTRAN), the multiple scattering calculations are based on the Discrete Ordinate (DISORT) method (Stamnes et al. 1988). The radiative transfer equation is solved for N discrete zenith angles to obtain N equations for N unknowns. These unknowns may be solved numerically. The MODTRAN single scattering radiances are computed separately from DISORT with inclusion of spherical geometry effects; the plane-parallel DISORT single scattering contributions are subtracted from the DISORT radiances for generation of the total radiance values. For the comparisons a beta version, MODTRAN4v2r0, was used, in which user-defined phase functions for cloud particles could be specified.

- Spherical Harmonics method

The Spherical Harmonic Discrete Ordinate Method SHDOM (Evans 1998) has been developed for modeling radiative transfer in inhomogeneous three-dimensional media. SHDOM uses an iterative procedure to compute the source function of the radiative transfer equation on a grid of points in space. The angular part of the source function is represented by a spherical harmonics expansion mainly because the source function is computed more efficiently in this way than in DISORT. A discrete ordinate representation is used in the solution process. The number of iterations increases with increasing single scattering albedo and optical thickness.

The intercomparison study demonstrated that SHDOM and DAK are suitable models for the calculations of narrow-band cloud reflectances. For a clear atmosphere all models showed small absolute differences relative to the reference model (Monte Carlo), while for a cloudy atmosphere considerably larger absolute differences were observed. The causes for the latter differences are due to numerical noise or differences in the multiple scattering calculations. The implementation of a user-defined phase function in MODTRAN4v2r0 (beta release) was a large improvement, it was still the least accurate model for the simulation of cloud reflectances in this study. On average MODTRAN simulations deviated less than 3% from the reference model, but for individual viewing angles in the principal plane the deviations can increase to about 30%. It was suggested that the differences in MODTRAN reflectances cannot be fully explained by the method for multiple scattering calculations (DISORT). Part of the observed differences may be explained by different or incorrect model parameterizations. However, MODTRAN has been further improved since the study by Roebeling et al. (2005). The DAK and SHDOM calculations were similar to Monte Carlo, with mean differences smaller than 3%. However, for individual cases the differences were occasionally much larger. A noticeable finding was that the Monte Carlo has a 3% bias as compared to SHDOM and DAK. This bias may be explained by differences in the treatment of the forward peak of the scattering phase function. Especially for large particles with a

strong forward peak this may cause significant differences in simulated reflectances. Beside these differences, Monte Carlo showed small non-systematic oscillations relative to SHDOM and DAK. These oscillations were largest for optically thick clouds ($\tau = 64$), for moderate particle sizes ($r_e = 10 \, \mu$m) and for large viewing zenith angles (75°). For these cases the number of multiple scattering events is large (up to 200) and the forward peak is strong, such that small differences in single scattering parameters can easily accumulate to large errors in the reflectances (±2%). Finally, the used version of SHDOM became unstable at certain optical thicknesses and effective radii. Comprehensive analysis showed that these instabilities occur at 0.63 and 1.61 μm wavelengths and that the problem disappeared again by choosing another optical thickness or effective radius.

Instrument errors

The solar channels of the satellite instruments covered in this ATBD are not calibrated on-board. For AVHRR the pre-flight calibration coefficients for the solar channels have been shown to be sometimes off by tens of percents (Heidinger et al. 2002). Recalibration using ground targets and other satellite instruments, such as MODIS, is thus crucial, and enhances the accuracy to typically 3-5%. The thermal channels are normally in a better shape because they are calibrated on board using blackbodies.

Errors in the observed reflectance translate non-linearly into errors in retrieved cloud properties, since the relationship between reflectance and cloud properties is non-linear. The CPP algorithm includes an error estimate for this retrieval error. We start from the functional relationship $R_{V,N} = f(\tau, r_e)$, where $R_{V,N}$ is the reflectance in the VIS or NIR channel. Derivation of this relation leads to:

$$\Delta R_{V,N} = \frac{\partial R_{V,N}}{\partial \tau}\bigg|_{r_e} \Delta \tau + \frac{\partial R_{V,N}}{\partial r_e}\bigg|_{\tau} \Delta r_e, \cdot \qquad (9)$$

where Δ denotes an error. The partial derivatives with respect to τ (r_e) are at constant r_e (τ), respectively. Equation (9) can be inverted to:

$$\Delta \tau = \frac{1}{F}\left(\frac{\partial R_N}{\partial r_e}\bigg|_{\tau} \Delta R_V - \frac{\partial R_V}{\partial r_e}\bigg|_{\tau} \Delta R_N \right); \cdot \qquad (10)$$

$$\Delta r_e = \frac{1}{F}\left(-\frac{\partial R_N}{\partial \tau}\bigg|_{r_e} \Delta R_V + \frac{\partial R_V}{\partial \tau}\bigg|_{r_e} \Delta R_N \right), \cdot \qquad (11)$$

with

$$\cdot F = \frac{\partial R_V}{\partial \tau}\bigg|_{r_e} \frac{\partial R_N}{\partial r_e}\bigg|_{\tau} - \frac{\partial R_V}{\partial r_e}\bigg|_{\tau} \frac{\partial R_N}{\partial \tau}\bigg|_{r_e} . \qquad (12)$$

The retrieval error in LWP follows directly from the errors in τ and r_e. These relations are applied in CPP with a 3% relative error in the VIS and NIR reflectance. The resulting error estimates relate to the propagation of reflectance errors into errors in retrieved cloud properties, and does not cover error sources discussed furtheron in this document.

Figure 4 shows the estimated retrieval errors for typical conditions, and their dependence on the cloud properties. Two important features are illustrated by this figure. First, the cloud optical thickness retrieval becomes highly uncertain for thick clouds as a result of the asymptotic relation between visible reflectance R and cloud optical thickness τ. The derivative $d\tau/dR$ increases with increasing τ, and for large values of τ a marginal change in visible reflectance causes a large increase in the retrieved cloud optical thickness. Second, the error in effective radius is generally between 2 and 3 μm, but becomes much larger for thin clouds. For this reason the retrieval of r_e for thin clouds is weighed towards a climatological value, as was discussed in Section 4.3. Figure 4 shows that errors get larger at high solar zenith angles, but not dramatically. Errors may increase more for particular parts of the phase function, e.g. the backward scattering peak or the rainbow.
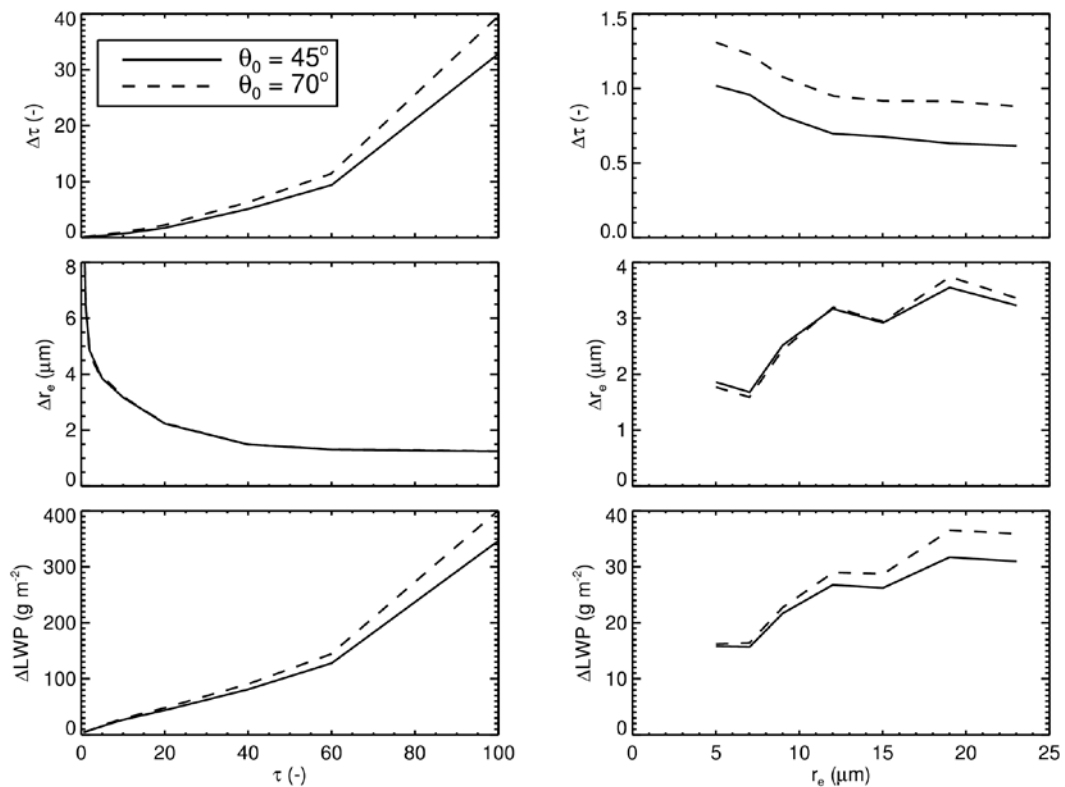

Figure 4 CPP retrieval errors as calculated using Equations (9) – (12). The errors in τ (top), r_e (middle), and LWP (bottom) are shown as a function of τ (left, with $r_e = 12$ μm kept constant) and r_e (right, with $\tau = 10$ kept constant). The calculations were done for $\theta_0 = 45°$ and $\theta_0 = 70°$, $\theta = 30°$ and $\varphi = 90°$, and are based on the 0.6-/1.6-μm channel combination.

Errors in ancillary data

A significant source of retrieval error is caused by uncertainties in surface reflectance α_s. This is illustrated in Figure 5, which displays the impact on retrieved LWP of a – realistic – 25% (relative) uncertainty in α_s. Deviations of α_s in the non-absorbing channel (left panels) mainly affect the retrieved cloud optical thickness. The impact is relatively largest for thin clouds because the TOA outgoing radiation over these clouds contains a considerable contribution from the surface. Deviations of α_s in the absorbing channel (right panels) mainly affect the retrieved effective radius. This impact is also largest for thin clouds, but due to the weighing with a climatological effective radius it is suppressed for the thinnest clouds. Hence, a maximum sensitivity is observed for an optical thickness around 5. In all cases LWP is more sensitive to uncertainties in α_s over the brighter land surfaces than over the darker ocean. Over ice- and snow-covered surfaces, with a typical 0.6-μm surface albedo of 0.8, the retrieval becomes extremely sensitive, with LWP deviations of over 100% (not shown in Figure 5).
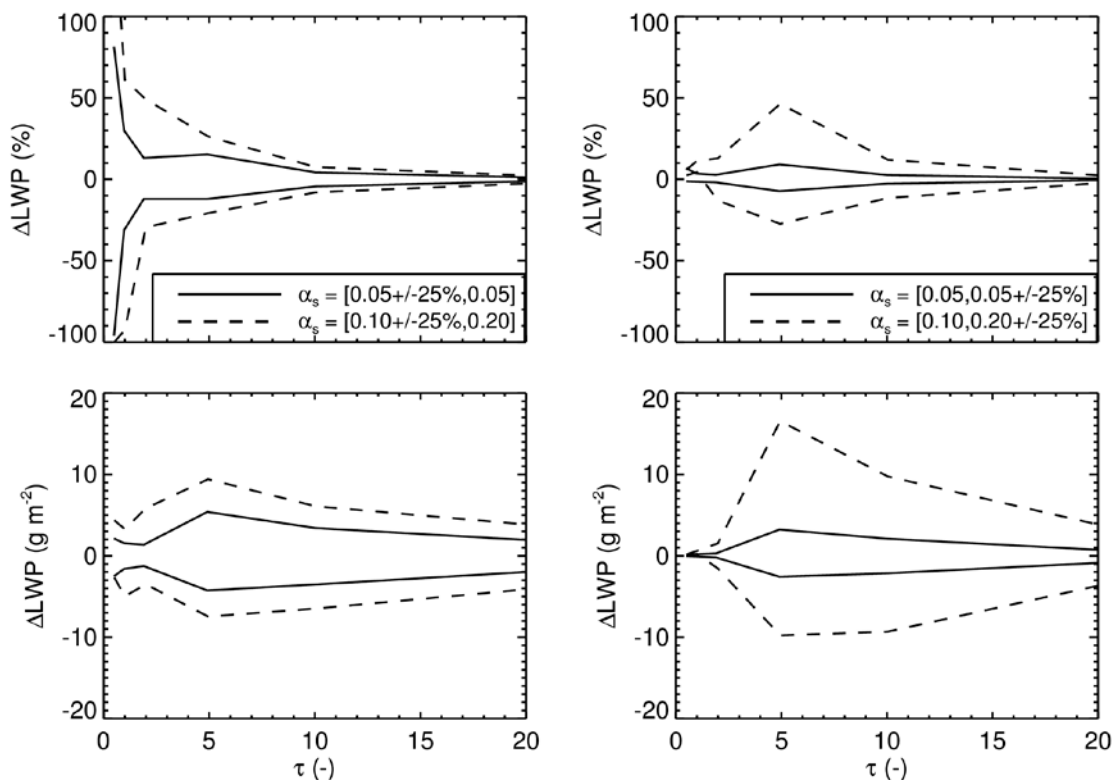

Figure 5 Sensitivity of retrieved LWP to uncertainties in surface reflectance. The curves show the relative (top panels) and absolute (bottom panels) deviation of LWP from the truth following from retrievals with a 25% increased or decreased surface reflectance in the 0.6-μm (left panels) and 1.6-μm (right panels) as a function of the true optical thickness. Two types of surfaces are distinguished: ocean with $\alpha_s = 0.05$ at 0.6 and 1.6 μm (solid lines) and land with $\alpha_s = 0.1$ at 0.6 and $\alpha_s = 0.2$ at 1.6 μm (dashed lines). The calculations were done for $\theta_0 = 45°$, $\theta = 30°$ and $\varphi = 90°$.

Another source of error is the ancillary data needed for the atmospheric correction. The largest impact is expected from uncertainties in the water vapour path and to a lesser extent the total ozone column. Errors in geolocation, solar angles and satellite angles can be assumed to be small, and hence their impact on cloud property retrievals is limited. Finally, the cloud mask, which is external input to the CPP algorithm (and thus considered here as ancillary data), is of importance. The cloud mask determines for which satellite pixels a retrieval is performed. It does not influence the retrieval itself, i.e. the level-2 products, but is does have impact on aggregated level-3 products. Typically, a more selective cloud mask (i.e. assigning less pixels cloudy) leads to a larger aggregated cloud optical thickness.

4.5. Practical Application

This section provides details on the AVHRR instruments and other input data used by the CPP algorithm.

4.5.1. AVHRR instrument

NOAA has launched a series of polar orbiting satellites that carry the AVHRR instrument. Recently, EUMETSAT also launched an AVHRR instrument on the METOP polar orbiting satellite. The AVHRR passive imager operates six channels at wavelengths between 0.5 and 12.0 µm. Table 1 summarizes the AVHRR channels used by CPP. Due to fundamental constraints, the near-infrared 1.6 µm and 3.7 µm channels are time-shared. On NOAA-16 (during the first two years of its life), NOAA-17, and METOP the 1.6-µm channel has been operated during the daylight part of the orbit, while the 3.7-µm channel was operated during night. All other NOAA satellites have only transmitted data from the 3.7-µm channel. The spatial resolution of all channels at nadir is around 1x1 km^2, but this is degraded to 5x4 km^2 for GAC-AVHRR.

Table 1: AVHRR channels used by CPP.

Channel	Central wavelength (µm)	Nominal spectral band (µm)
1	0.63	0.58 - 0.68
3a [a)]	1.61	1.58 - 1.64
3b [a)]	3.74	3.55 - 3.93
4	10.8	10.30 - 11.30

[a)] Only one NIR channel at the same time can be transmitted to the ground.

4.5.2. Input data

In this section, the input data used to run the CPP algorithms are described.

Radiances

The CPP algorithm needs radiances from the 0.6-µm, the 1.6-µm or 3.7-µm , and the 10.8-µm channels.

Solar and satellite angles

The CPP algorithm requires the solar zenith angle θ_0, the satellite viewing zenith angle θ, and the relative sun-satellite azimuth angle ϕ. These angles are calculated by the NWC-SAF software and provided as input to CPP.

Cloud mask

A cloud mask is needed to decide for which pixels a cloud physical properties retrieval will be attempted. The cloud mask of the NWC-SAF is used for this purpose (see RD-1). The CPP retrievals are run for pixels classified as *cloud contaminated* or *cloud filled*.

Cloud-top height and temperature

CPP has a built-in retrieval of cloud-top height and temperature as described in Section 4.3. In the future the use of the CTTH product from NWC-SAF (RD-2) will be considered.

Surface albedo

Over land this is prescribed from a 5-year mean MODIS 0.6- and 1.6-μm snow-free gap-filled white-sky surface albedo database with 16-day resolution (Moody et al., 2004, 2008). This database was chosen because: (i) it is a frequently used and well recognized dataset; (ii) it contains the spectral channels needed for CPP AVHRR and VIIRS processing; (iii) it has global extension and (iv) it is gap-filled. Over ocean the surface albedo is assumed to be 0.05 at both 0.6 μm and 1.6 μm.

Surface emissivity

For the 3.7-μm retrieval, a climatology compiled from four years of the MODIS-based surface emissivity database by Seemann et al. (2008) is used over land, while over ocean the surface emissivity is set to 0.98. The motivation for chosing this dataset was similar as for the surface albedo dataset. Another advantage is that the surface albedo and surface emissivity datasets are consistently based on MODIS observations.

Surface temperature

This is needed only for the 3.7-μm retrieval. It is obtained from NWP operational data.

Water vapour path

For the atmospheric correction a water vapour path from NWP operational data is used. It is also possilbe to use a climatology based on ECMWF ERA-Interim data.

5. Assumptions and Limitations

In this section some of the assumptions and limitations associated with the retrieval algorithms are listed. There are also general limitations related to the characteristics of the satellite instruments. For example, GAC-AVHRR has a nominal resolution of 5x4 km^2, compared to 1x1 km^2 for LAC-AVHRR. A coarser resolution gives rise to systematic biases in

the derived cloud physical properties, as outlined below. Also, polar orbiters have only two overpasses per day in the tropics (of which one during nighttime) and up to $\approx$8 near the poles. Thus, coverage of the diurnal cycle of cloud properties is limited.

Specific limitations for the cloud physical products include:

- The derivation of cloud physical properties from reflected solar radiation is dependent on the availability of daylight. This means that no retrievals can be done during night time.

- Cloud retrievals are performed assuming that clouds are plane parallel. This is true only in a minority of cases, which implies that retrieval errors become larger as clouds deviate from being plane parallel. Especially convective clouds can be problematic, as they frequently have illuminated and shadowed sides (see, e.g., Marshak et al. 2006). Broken cloud fields can also cause problems for retrieving cloud properties, since a passive satellite sensor measures an averaged radiance of the cloudy and cloud-free part of a pixel. The error made in these cases is among others dependent on the contrast between clouds and underlying surface, the true properties of the cloud, and the cloud fraction within the sampling resolution of the instrument (Oreopoulos and Davies 1998; Coakley et al. 2005; Wolters et al. 2010).

- The retrieval is highly problematic over very bright surfaces, particularly ice and snow, as the visible reflectance from clouds is similar to that from the surface.

- Unlike active satellite instruments, which can derive cloud profile information, retrievals from passive satellite instruments are limited by the fact that the obtained signal emanates from the integrated profile. Since near-infrared radiation is only penetrating into the cloud to a certain depth (due to absorption by cloud particles), the retrieved cloud phase and effective radius are representative for the upper part of the cloud (Platnick 2001). The penetration depth depends on the amount of absorption by cloud particles, which is increasing with wavelength. This means that the retrieved CPH and r_e depend on which NIR spectral channel is used (in our case 1.6 or 3.7 μm). See, for example, Rosenfeld et al. (2004) for a discussion on pros and cons of the use of different NIR channels.

- In the derivation of Equation (2) for LWP and IWP it is assumed that the cloud particle effective radius does not vary with height. In reality this assumption is not satisfied. For example, liquid water clouds often obey adiabatic theory leading to a slightly different relation for LWP, in which the factor 2/3 is replaced by 5/9. Thick ice clouds often have small ice crystals at the top, which are not representative of the full vertical extent. As a consequence, IWP can be underestimated in these cases.

- Aerosols are not considered in the CPP retrieval. This assumption is usually justified because aerosols reside below or within the cloud and their optical thickness is small compared to that of the cloud. However, if the aerosols reside above the cloud and if they are sufficiently absorbing, they can significantly lower the visible reflectance. The effect on the retrievals depends on the channel combination used and on the aerosol properties (Haywood et al. 2004). The impact is strongest for the 1.6-μm channel, with a possible understimation of r_e by several microns. For the 3.7-μm channel, the impact is smaller and can be an overestimation of r_e. Cloud optical thickness generally has a low bias.

- Precipitation may have an effect on cloud property retrievals in case the radiation penetrates sufficiently deep into the cloud to be affected by the (large) precipitating droplets. Retrievals with the 1.6-μm channel are expected to be most sensitive to this, but

synthetic studies (e.g., Zinner et al. 2010) have not indicated significant impact on the effective radius retrieval.

- Many assumptions are made for the calculation of LUTs with DAK. These include: the absence of aerosols, the location of the cloud between 1 and 2 km height, the specific habits and resulting phase functions of ice crystals, and the type and width of water droplet effective radius distributions. The necessity of these assumptions is an illustration of the heavily underconstrained nature of the cloud physical properties retrieval principle.

6. References

Ackerman, S.A., W.L. Smith, R.E. Revercomb, and J.D. Spinhirne, 1990: The 27–28 October 1986 FIRE IFO Cirrus Case Study: Spectral Properties of Cirrus Clouds in the 8–12 µm Window, *Mon. Wea. Rev.*, **118**, 2377-2388.

Anderson, G. P., S. A. Clough, F. X. Kneizys, J. H. Chetwynd, and E. P Shettle, 1986: AFGL Atmospheric Constituent Profiles (0-120km). Tech. Rep. AFGL-TR-86-0110, 43 pp.

Berk, A., G. P. Anderson, P. K. Acharya, J. H. Chetwynd, L.S. Bernstein, E. P. Shettle, M. W. Matthew, and S. M. Adler-Golden, 2000: MODTRAN4 Version 2 Users Manual. Technical report, Air Force Materiel Command, Air Force Research Laboratory, Space Vehicles Directorate, Hanscom AFB, MA 01731, USA.

Chandrasekhar S., 1960: *Radiative Transfer*, New York, Dover, 393 pp.

Coakley, J. A., M. A. Friedman, and W. R. Tahnk, 2005: Retrieval of cloud properties for partly cloudy imager pixels, *J. Atmos. Ocean. Technol.,* **22** , 3–17.

Davis, J. M., T. B. McKee, and S. K. Cox, 1985: Application of the Monte Carlo method to problems in visibility using a local estimate: an investigation. *Appl. Optics*, **24**, (19), 3193-3205.

De Haan, J. F., P. Bosma, and J. W. Hovenier, 1987: The adding method for multiple scattering calculations of polarized light, *Astron. Astrophys.*, **183**, 371-391.

Evans, K. F., 1998: The Spherical Harmonics Discrete Ordinate, Method for Three-Dimensional Atmospheric Radiative Transfer. *J. Atmos. Sci.*, **55**, 429-446.

Gao, B.-C. and W. J. Wiscombe, 1994: Surface-induced brightness temperature variations and their effects on detecting thin cirrus clouds using IR emission channels in the 8-12 micron region. *J. Appl. Met.*, **33**, 568-570.

Greuell, W., E. van Meijgaard, J.F. Meirink, and N. Clerbaux, 2011: Evaluation of model predicted top-of-atmosphere radiation and cloud parameters over Africa with observations from GERB and SEVIRI, *J. Climate*, **25**, 4015 – 4036, doi:10.1175/2011JCLI3856.1.

Greuell, W. and R. A. Roebeling, 2009: Towards a standard procedure for validation of satellite-derived Cloud Liquid Water Path: a study with SEVIRI data, *J. Appl Meteor. Climatol.,* **48**, 1575 – 1590, doi:10.1175/2009JAMC2112.1.

Han, Q., W. B. Rossow, and A. A. Lacis, 1994: Near-Global Survey of Effective Droplet Radii in Liquid Water Clouds Using ISCCP Data. *J. Climate,* **7**, 465-497.

Haywood, J.M., S.R. Osborne, S.J. Abel, 2004: The effect of overlying absorbing aerosol layers on remote sensing retrievals of cloud effective radius and cloud optical depth, *Quart. J. Roy. Meteorol. Soc.*, **130**, 779-800, doi: 10.1256/qj.03.100.

Heidinger, A.K., C. Cao, and J.T. Sullivan, 2002: Using Moderate Resolution Imaging Spectrometer (MODIS) to calibrate advanced very high resolution radiometer reflectance channels, *J. Geophys. Res.*, **107**, D23, 4702, doi:10.1029/2001JD002035.

Hess, H, R. B. A. Koelemeijer, and P. Stammes, 1998: Scattering matrices of imperfect hexagonal crystals. *J. Quant. Spectrosc. Radiat. Transfer*, **60**, 301–308.

Jolivet, D., and A. J. Feijt, 2003: Cloud thermodynamic phase and particle size estimation using the 0.67 and 1.6 micron channels from meteorological satellites. *Atm. Chem. and Phys.*, **3**, 4461-4488.

Knap, W. H., L. C. Labonnote, G. Brogniez, and P. Stammes, 2005: Modeling total and polarized reflectances of ice clouds: evaluation by means of POLDER and ATSR-2 measurements. *Appl. Optics*, **44**, 4060-4073.

Macke, A., D. Mitchell, and L. von Bremen, 1999: Monte Carlo radiative transfer calculations for inhomogeneous mixed phase clouds. *Phys. Chem. Earth*, **24-3**, 237-241.

Marshak, A., S. Platnick, T. Várnai, G. Wen, and R. F. Cahalan, 2006: Impact of three-dimensional radiative effects on satellite retrievals of cloud droplet sizes, *J. Geophys. Res.*, **111** , 9207–9218.

McFarquhar, G.M. and A.J. Heymsfield, 1998: The definition and significance of an effective radius for ice clouds, *J. Atmos. Sci.*, **55**, 2039-2052.

Meirink, J.F., R.A. Roebeling and P. Stammes, 2009: Atmospheric correction for the KNMI Cloud Physical Properties retrieval algorithm, KNMI publication: TR-304, 17/2/2009, pp22.

Minnis, P., K. N. Liou, and Y. Takano, 1993: Inference of Cirrus Cloud Properties Using Satellite-observed Visible and Infrared Radiances. Part I: Parameterization of Radiance Fields. *J. Atmos. Sci.*, **50**, 1279–1304.

Moody, E. G., M. D. King, S. Platnick, C. B. Schaaf, F. Gao, 2004: Spatially complete global spectral surface albedos: Value-added datasets derived from Terra MODIS land products. *IEEE Trans. Geosci. Remote Sens.*, **43**, 144-158.

Moody, E.G., M.D. King, C.B. Schaaf, and S. Platnick, 2008: MODIS-Derived Spatially Complete Surface Albedo Products: Spatial and Temporal Pixel Distribution and Zonal Averages. *J. Appl. Meteor. Climatol.*, **47**, 2879–2894.

Nakajima, T., and M. D. King, 1990: Determination of the Optical Thickness and Effective Particle Radius of Clouds from Reflected Solar Radiation Measurements. Part 1: Theory. *J. Atmos. Sci .*, **47**, 1878-1893.

Nakajima, T. Y., and T. Nakajima, 1995: Wide-Area Determination of Cloud Microphysical Properties from NOAA AVHRR Measurements for FIRE and ASTEX regions. *J. Atmos. Sci,* **52**, 4043 – 4059.

Oreopoulos, L., and R. Davies, Plane parallel albedo biases from satellite observations. part I: Dependence on resolution and other factors, 1998: *J. Climate*, **11** , 919–932.

Platnick, S., 2001: A superposition technique for deriving mean photon scattering statistics in plane-parallel cloudy atmospheres, *J. Quant. Spectrosc. Radiat. Transfer*, **68**, 57-73

Platnick, S., King, M. D., Ackerman, S. A., Menzel, W. P., Baum, B. A., Riedi, J. C., Frey, R. A., 2003: The MODIS cloud products: Algorithms and examples from Terra. *IEEE Trans. Geosci. Remote Sens.*, **41**, 459-473.

Roebeling, R. A., 2008: Cloud Physical Properties Retrieval for Climate Studies using SEVIRI and AVHRR data, PhD Thesis, Wageningen University, The Netherlands, 160pp. Available from http://www.knmi.nl/publications.

Roebeling, R. A., A. Berk, A. J. Feijt, W. Frerichs, D. Jolivet, A. Macke, and P. Stammes, 2005: Sensitivity of cloud property retrievals to differences in narrow band radiative transfer simulations, KNMI Scientific Report, WR 2005-02, Royal Netherlands Meteorological Institute, De Bilt, the Netherlands, 27 pp. Available from http://www.knmi.nl/publications.

Roebeling, R. A., A. J. Feijt, and P. Stammes, 2006: Cloud property retrievals for climate monitoring: implications of differences between SEVIRI on METEOSAT-8 and AVHRR on NOAA-17, *J. Geophys. Res.*, **111**, D20210, doi:10.1029/2005JD006990.

Roebeling, R.A., H. M. Deneke, and A. J. Feijt, 2008: Validation of cloud liquid water path retriveals from SEVIRI using one year of CloudNET observations, *J. Appl. Meteorol. Clim.*, **47**, 206-222.

Roebeling, R. A. and E. van Meijgaard, 2009: Evaluation of the Daylight Cycle of Model-Predicted Cloud Amount and Condensed Water Path over Europe with Observations from MSG SEVIRI, *J. Climate*, **22**, 1749 – 1766, doi:10.1175/2008JCLI2391.1.

Rosenfeld, D., E. Cattani, S. Melani, and V. Levizzani, 2004: Considerations on daylight operation of 1.6-versus 3.7-μm channel on NOAA and Metop satellites. *B. Am. Meteorol. Soc.*, **85**, 873–881.

Rossow, W.B., and R.A. Schiffer, 1999: Advances in understanding clouds from ISCCP. *B. Am. Meteorol. Soc.*, **80**, 2261-2287.

Seemann, S.W., E. E. Borbas, R. O. Knuteson, G. R. Stephenson, H.-L. Huang, 2008: Development of a Global Infrared Land Surface Emissivity Database for Application to Clear Sky Sounding Retrievals from Multi-spectral Satellite Radiance Measurements, *J. Appl. Meteor. Climatol.*, **47**, 108-123.

Stammes, P., 2001: Spectral radiance modeling in the UV-Visible range. IRS 2000: Current problems in Atmospheric Radiation, edited by W.L. Smith and Y.M. Timofeyev, pp 385-388, A. Deepak Publ., Hampton, Va.

Stamnes, K., S. C Tsay, W. Wiscombe, and K Jayaweera, 1988: Numerically stable algorithm for discrete ordinate method radiative transfer in multiple scattering and emitting layered media. *Appl. Optics,* **27**, 2502-2509.

Stephens, G. L., 1978: Radiation profiles in extended water clouds: II. Parameterization schemes. *J. Atmos. Sci.*, **35**, 2123-2132.

Stephens, G. L. and C. D. Kummerow, 2007: The Remote Sensing of Clouds and Precipitation from Space: A Review. *J. Atmos. Sci.*, **64** , 3742–3765.

Warren, S. G., 1984: Optical constants of ice from the ultraviolet to the microwave. *Appl. Optics*, **23**, 1206–1225.

Watts, P. D., C. T. Mutlow, A. J. Baran, and A. M. Zavody, 1998: Study on Cloud Properties derived from Meteosat Second Generation Observations, Final Report, EUMETSAT ITT no. 97/181.

Wolters, E. L .A., H. M. Deneke, B. J. J. M. van den Hurk, J. F. Meirink, and R. A. Roebeling, 2010: Broken and inhomogeneous cloud impact on satellite cloud particle effective radius and cloud-phase retrievals, *J. Geophys. Res.*, **115**, doi:10.1029/2009JD012205.

Wolters, E. L. A., R.A. Roebeling, and A. J. Feijt, 2008: Evaluation of cloud-phase retrieval methods for SEVIRI onboard Meteosat-8 using ground-based lidar and cloud radar data, *J. Appl. Meteorol. Clim.*, **47**, 1723-1738, doi:10.1175/2007JAMC1591.1.

Wolters, E. L. A., R. A. Roebeling, and P. Stammes, 2006: Cloud reflectance calculations using DAK: study on required integration points, KNMI Technical Report, TR-292, Royal Netherlands Meteorological Institute, De Bilt, The Netherlands, 17 pp. Available from http://www.knmi.nl/publications.

Zinner, T., G. Wind, S. Platnick, and A.S. Ackerman, 2010: Testing remote sensing on artificial observations: impact of drizzle and 3-D cloud structure on effective radius retrievals, *Atmos. Chem. Phys.*, **10**, 9535-9549, doi:10.5194/acp-10-9535-2010.